Breakdown insensitive acceleration regime in a metamaterial accelerating structure

Dillon Merenich, Brendan Leung, Gaurab Rijal, and Xueying Lu*
Northern Illinois University, DeKalb, Illinois 60115, USA

Scott Doran, Gongxiaohui Chen, Wanming Liu, Chunguang Jing, John Power, Charles Whiteford, and Eric Wisniewski
Argonne National Laboratory, Lemont, Illinois 60439, USA

(Received 9 September 2023; accepted 12 March 2024; published 8 April 2024)

A new regime in radiofrequency (rf) breakdown, named the breakdown insensitive acceleration regime (BIAR), was observed in an 11.7 GHz metamaterial structure for wakefield acceleration driven by rf pulses with a duration of a few nanoseconds. In the BIAR, rf breakdown occurs without interrupting potential beam acceleration, resulting in greater resilience to breakdown. We have investigated the possibility that BIAR can support higher gradients by characterizing the breakdown in a high-power test. The peak gradient reached 190 MV/m when the structure was powered by 6 ns long rf pulses with 115 MW peak power. The short rf pulses were extracted from 65 MeV electron bunch trains with a total charge of up to 210 nC. This work has revealed the benefits of short-pulse acceleration by characterizing rf breakdown in the previously unexplored parameter space.

DOI: 10.1103/PhysRevAccelBeams.27.041301

Radiofrequency (rf) breakdown is the fundamental limitation to reaching higher accelerating gradients in particle accelerators. Exploring novel approaches to increase the gradient beyond the rf breakdown limit is critical to future energy-frontier colliders [1–3] and has been the goal of advanced accelerators research [4]. The plasma-based wakefield acceleration approaches [5–11], including both beam-driven plasma wakefield acceleration and laser wakefield acceleration, remove the limitation by using plasmas, which are not susceptible to rf breakdown, as the accelerating media. An alternative scheme, the structure-based wakefield acceleration (SWFA) [1,4,12,13], tackles the problem of rf breakdown by confining the microwave energy in a short and intense rf pulse. Colliders [14] have been proposed based on this concept. In SWFA, the wakefield is excited by a drive bunch traversing an rf structure in vacuum. The generated wakefield, as a short rf pulse, can be used to accelerate a trailing witness bunch in the same structure (collinear wakefield acceleration) or in a separate structure (two-beam acceleration). The pulse length in SWFA can reach only a few nanoseconds, much shorter than the typical pulse length in conventional rf accelerators that ranges from a few hundred nanoseconds to a few microseconds. Experimental studies on high-gradient rf structures operating with varied pulse lengths [15–20], and demonstrations of high-power extraction [21–26] and high-gradient generation [27–31] in SWFA have revealed the potential benefits of using short pulses. In this paper, we conducted a short-pulse SWFA experiment and observed a new acceleration regime, the breakdown insensitive acceleration regime (BIAR), where rf breakdown occurs without interrupting potential beam acceleration. This new regime sheds light on the physics of breakdown mitigation using short pulses, and the advantages of short-pulse acceleration can be extended beyond the SWFA scheme to other accelerator applications including colliders and light sources.

The physics understanding of rf breakdown has been highly sought after and greatly deepened in the last few decades through theoretical modeling [32–39] and experimental studies [15–20,27,28,40–57]. These studies have identified common breakdown initiators, including pulsed heating, multipacting, and field emission. According to the empirical scaling law [18] of the breakdown rate (BDR) with the gradient E_a and the pulse length t_p, as $E_a^{30} \times t_p^5/\mathrm{BDR} =$ constant, operating with short pulses can potentially reduce the BDR. However, our understanding of rf breakdown with nanosecond-long pulses is based on the extrapolation of data from studies within a parameter space corresponding to pulse lengths suitable for conventional accelerators. In pioneering short-pulse breakdown studies [15,16,55], the gradient achieved was limited by available power levels when the

*xylu@niu.edu
Also at Argonne National Laboratory, Lemont, Illinois 60439, USA.

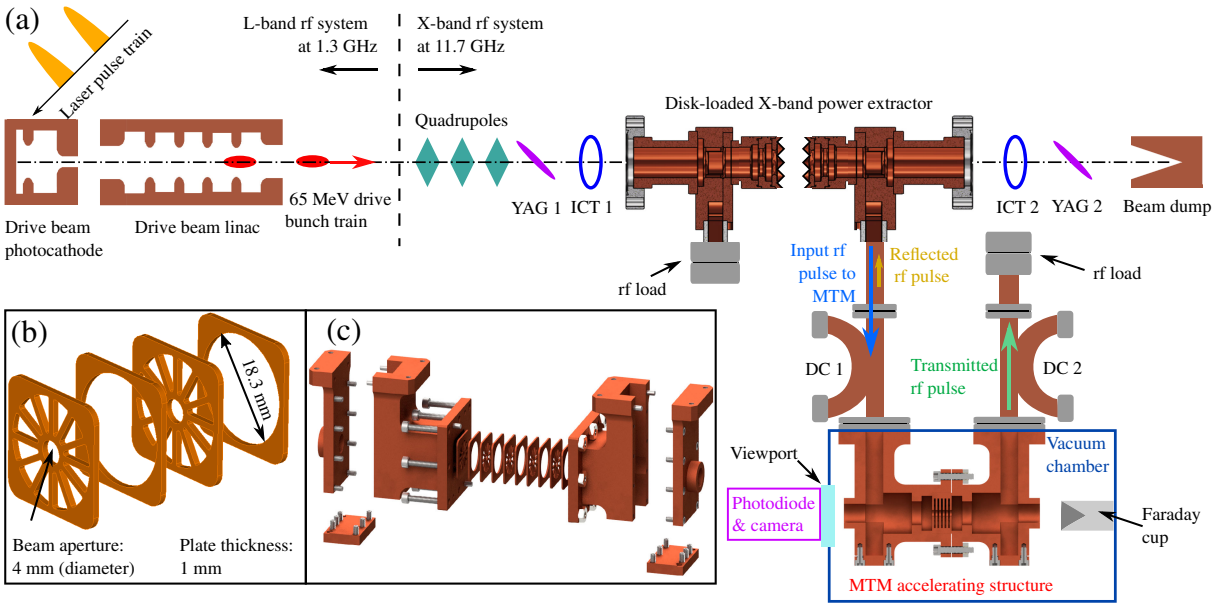

FIG. 1. Schematic of the breakdown test of the 11.7 GHz metamaterial (MTM) accelerating structure at the Argonne Wakefield Accelerator (AWA). (a) Block diagram of the AWA 65 MeV drive electron beamline and the breakdown test stand. "YAG" denotes yttrium aluminum garnet mirrors for measurement of the beam transverse profile, "ICT" denotes integrating current transformers for measurement of the bunch-train charge, and "DC" denotes directional couplers for measurement of the rf signals. (b) Unit cell design of the MTM structure, with one "wagon wheel" plate and one spacer plate per period. (c) Exploded view of the six-cell MTM structure, with power couplers at both ends.

pulse length was below a few tens of nanoseconds. In this study, we conducted a high-power test on an 11.7 GHz metamaterial (MTM) accelerating structure using the SWFA approach at the Argonne Wakefield Accelerator (AWA). The input rf pulses to the MTM structure were generated using a power extractor excited by high-charge electron bunch trains. The MTM structure is designed for two-beam acceleration, while this study is an rf breakdown test with no witness beam.

The MTM structure was designed to address challenges arising from the short-pulse length, due to the trade-off between a short structure filling time t_f required to accommodate the short-pulse regime, and a high gradient in the steady state E_{steady} (when the pulse length $t_p \gg t_f$). This trade-off makes the choice of the group velocity v_g of the structure critical since a short filling time $t_f = L/|v_g|$ prefers a high group velocity, while a high steady-state gradient (which is different from the transient gradient) prefers a low group velocity, as $E_{\text{steady}} = \sqrt{4k_L P/|v_g|}$, where P is the steady-state input rf power, $k_L = (\omega/4) \times (r/Q)$ is the structure loss factor, $\omega/(2\pi)$ is the rf frequency, and r/Q is the shunt impedance per unit length over the quality factor. A higher shunt impedance typically results in a reduced group velocity. The MTM structure with a negative group velocity, when compared to accelerating structures at the same frequency with positive group velocities [30,58], has a higher shunt impedance with the same group velocity magnitude [24,59] and can thereby reach a higher gradient with the same input rf power in the short-pulse regime. Examples of such comparisons can be found in Ref. [24]. MTM structures are subwavelength periodic structures with exotic features such as simultaneously negative effective permittivity and permeability [60,61]. The MTM structure in this experiment is a one-dimensional MTM structure, with a period of 2 mm in the longitudinal direction (or the beam direction). This period is much smaller than the free-space wavelength of 25.6 mm at 11.7 GHz. Each unit cell comprises one copper "wagon wheel" plate and one copper spacer plate, as shown in Fig. 1(b). The group velocity is $-0.012c$ (where c is the speed of the light) with $r/Q = 21$ kΩ/m to maximize the gradient with a 6 ns long input pulse. A blowout view of the complete six-cell structure is shown in Fig. 1(c), including two power couplers as the input and output ports. More information about the structure design and low-power microwave measurements can be found in the Appendix.

A high-power test was conducted to study the high-gradient performance of the MTM structure and to study short-pulse rf breakdown physics. Figure 1(a) shows the experimental setup. Electron bunch trains spaced at 1.3 GHz (L-band) were produced at the photocathode from laser pulse trains at 2 Hz, accelerated to 65 MeV in the L-band linac and then sent through the X-band metallic disk-loaded power extractor [25]. The total charge in eight-bunch trains reached 210 nC, with a charge transmission of nearly 100%, as verified by the integrating current transformers. The extracted rf pulse has a FWHM duration of 6 ns, and a center frequency of 11.7 GHz (as the

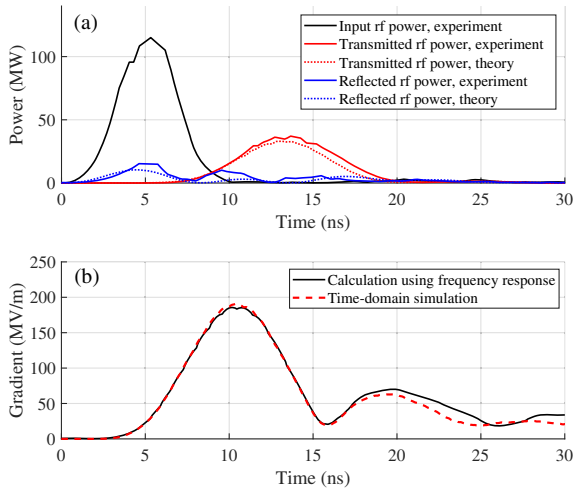

FIG. 2. Sample waveforms from the high-power test of the MTM structure during normal operation. (a) Measured input, transmitted, and reflected rf pulses in solid lines, benchmarked against theoretically calculated waveforms in dotted lines. (b) Gradients obtained using two methods were in good agreement: Calculation using the frequency-domain response of the structure (solid black) and direct time-domain simulation (dashed red).

ninth harmonic frequency of 1.3 GHz for coherent addition of the wakefield extracted from the bunch trains). The extracted rf pulses were then transmitted through a waveguide to the input port of the MTM structure. The MTM structure was installed in a vacuum chamber equipped with breakdown diagnostics. The input and reflected rf signals were measured by the directional couplers before and after the structure, as DC1 and DC2 in Fig. 1(a), respectively. A Faraday cup was placed close to one end of the structure for dark current measurement. Light diagnostics were set up, including one photodiode detector and one camera at the viewport.

The MTM structure underwent rf conditioning to a peak input power of 115 MW, resulting in a peak gradient of 190 MV/m. The sample waveforms are shown in Fig. 2(a), including the input, transmitted, and reflected rf power traces. The measured traces for the transmitted and reflected rf signals were benchmarked against the corresponding theoretical waveforms. The theoretical waveforms were generated as the convolution of the measured input rf waveform and the inverse Fourier transform of the structure scattering parameters (or S parameters [62]). The electromagnetic field in the MTM structure is intricate, including not only the eigenfrequency component at 11.7 GHz but also additional components originated from the 0.2 GHz bandwidth of the short-input pulse. The gradient is calculated through two approaches with good agreement, utilizing complementary information from frequency-domain and time-domain simulations in the CST Studio Suite [63]. The first approach involves utilizing the simulated frequency spectrum of the electric field to reconstruct the temporal evolution

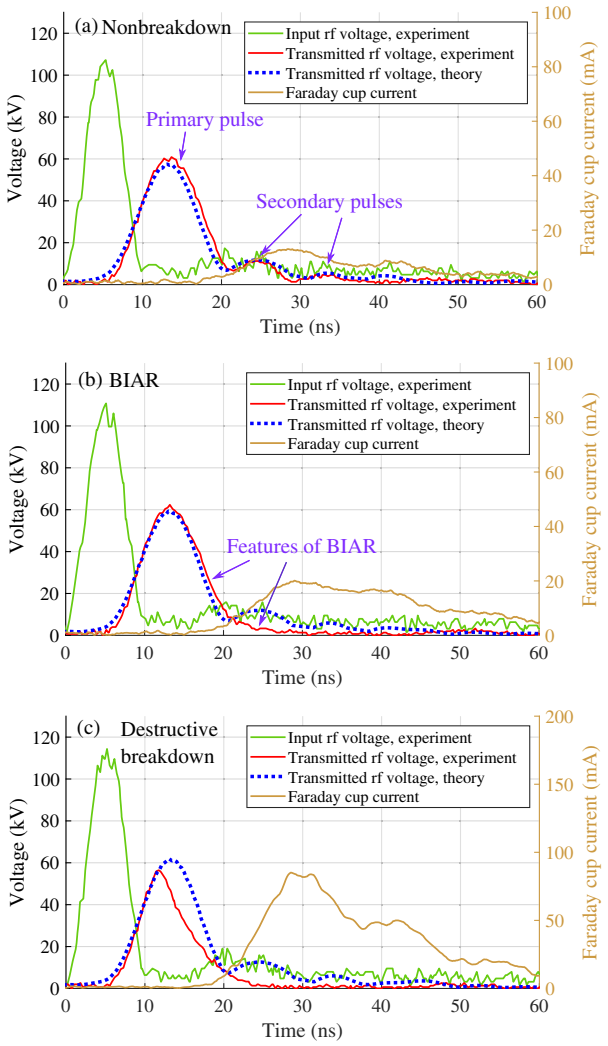

FIG. 3. Three types of events observed: (a) A nonbreakdown event. (b) A BIAR breakdown event. (c) A destructive breakdown event. The figures illustrate the input and transmitted rf voltage traces and the Faraday cup current data. The rf voltage waveforms (instead of the rf power waveforms in Fig. 2), whose amplitudes scale as $(\text{rf power})^{1/2}$, are presented to improve the discernibility of the secondary pulses.

of the gradient. The second approach involves a direct time-domain simulation. The peak surface electric field is estimated to be approximately 1 GV/m, with the ratio of the peak surface field to the gradient simulated as 5, following the methodology detailed in Ref. [64].

Three types of events were observed as shown in Fig. 3, and we name them nonbreakdown events, BIAR breakdown events, and destructive breakdown events, respectively. The primary distinguishing factor lies in whether and when the breakdown starts. The short-input pulse generates an unconventional time structure in the transmitted pulse, with a primary pulse and secondary pulses, both in the fundamental mode of the MTM structure. The primary pulse, characterized by higher power and longer duration

compared to the secondary pulses, can be used for the acceleration of a potential witness bunch by the two-beam acceleration technique. Conversely, the secondary pulses do not play a critical role in the acceleration process. Figure 3(a) shows the waveforms for a nonbreakdown event, where the measured transmitted rf voltage waveform is in excellent agreement with the theoretical waveform. In comparison, for the two types of breakdown events, the measured transmitted rf waveforms deviate from the theoretical waveforms, as the theory assumes the absence of breakdown. For the destructive breakdown [Fig. 3(c)], both the primary and the secondary pulses are interrupted, while for the BIAR breakdown [Fig. 3(b)], only the secondary pulses are interrupted, and the acceleration of a potential witness beam during the unaffected primary pulse remains achievable. We classify an event with a voltage decrease of over 5% in the primary pulse as a destructive breakdown event. For breakdown events with longer pulses, the transmitted power could drop to zero. Destructive breakdown does not mean damage to the structure but rather interruptions to the rf pulses. Details about the breakdown event identification and statistical analysis showing the bimodal features between the two types of breakdown are presented in the Appendix.

More than 3×10^5 pulses were recorded in two phases, the conditioning and testing phases, as shown in Fig. 4(a). The MTM structure remains intact after the high-power test, with a slight improvement in the rf transmission attributed to rf conditioning. In contrast to the previous

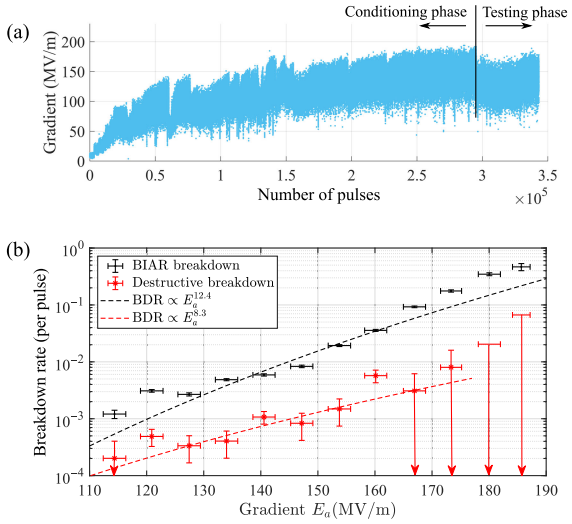

FIG. 4. Breakdown test results. (a) Gradient history of the breakdown test, divided into two phases: the conditioning phase and the testing phase. (b) Breakdown rate (BDR) in the testing phase plotted against the gradient E_a, for both the BIAR breakdown (black) and the destructive breakdown (red). Fitted results are shown using dashed lines in their corresponding colors. No destructive breakdown events were observed in the two highest gradient bins, where limits of BDR are provided but not included in generating the fitting curve.

klystron-powered breakdown tests, we generated the input rf pulses (with a peak power of P_{in}) as the wakefield extracted from the electron bunch trains with a total charge of Q_{tot}. Therefore, P_{in} scales according to $P_{\text{in}} \propto Q_{\text{tot}}^2$, and the variation in the gradient is a result of fluctuations in Q_{tot}. To facilitate the BDR analysis with varying gradient values, we divided the data into a series of bins. Figure 4(b) presents the BDR from the data collected in the testing phase for both breakdown types. The destructive BDR is approximately 1 order of magnitude lower than the BIAR BDR, indicating that acceleration in the short-pulse regime could lead to fewer interruptions of operation. Different breakdown damage behaviors between short and long pulses were reported in laser-induced breakdown [65]. In the case of rf breakdown, the destructive breakdown was observed at high gradients in the primary pulse and is thus likely associated with the field emission process [66,67]. Multipacting may have a higher contribution to the BIAR breakdown, observed at lower gradients [68–70] in the secondary pulses. Consequently, the BDR behaviors differ between the two breakdown types and also differ from the extrapolation of the empirical scaling law obtained from breakdown studies with longer pulses.

The observed resilience to breakdown in the BIAR is likely related to confining the rf power in a short duration, so breakdown-related physics processes may not fully develop. In the multipacting process, the rate of change of the gradient is one to 2 orders of magnitude higher in this experiment than in similar-frequency rf structures tested with longer pulses. This implies that each potential multipacting resonance mode has significantly less time to develop in the short-pulse regime [54]. Plasma generation at the structure surface could also trigger breakdown, while the plasma expansion would take on the order of tens of nanoseconds to block rf transmission [71,72]. Another characteristic of the short-pulse rf breakdown is that no light was observed by either the photodiode or by the camera throughout the experiment, whereas light emission is a common breakdown indicator in accelerating structures with longer pulses. On the modeling side, performing multiphysics simulations of short-pulse breakdown phenomena is one interesting future direction. On the experimental side, two-beam acceleration experiments to demonstrate the acceleration of a witness beam in the BIAR regime and to study the effect of beam loading on the BIAR breakdown are valuable and planned at AWA. Although not yet suitable for realistic machines, new structure designs with multiple optimization goals show promise in achieving gradients of up to 500 MV/m with the ratio of the surface field to the gradient reduced and the BDR reduced as a result at lower operating gradients. More detailed characterization of dark electrons is under development with multiple Faraday cups.

The SWFA approach has great advantages in generating high-power nanosecond-long rf pulses and in achieving

high-gradient acceleration, and SWFA-based breakdown tests can provide insights into rf breakdown physics in a previously unexplored parameter space. Short-pulse acceleration can lead to a dramatic improvement in the gradient and rf-to-beam efficiency in a range of accelerator applications, including linear colliders, injectors for circular colliders [73], and x-ray free electron lasers [74,75]. Complementary approaches capable of generating nanosecond-long pulses using active pulse compressors [76,77] and using frequency-chirped microwave sources with passive pulse compressors [78,79] also contribute to further advances of short-pulse acceleration.

This research was supported by the U.S. Department of Energy, Office of Science, Office of High Energy Physics under Award No. DE-SC0021928, and the Chicagoland Accelerator Science Traineeship (CAST) program sponsored by the U.S. DOE Award No. DE-SC0020379. The work at the AWA was funded through the U.S. Department of Energy, Office of Science under Contract No. DE-AC02-06CH11357.

APPENDIX

1. Metamaterial structure design

The metamaterial (MTM) accelerating structure in this experiment is designed as a clamped structure with the wagon wheel plates and the spacer plates and two power couplers. The assembled structure is shown in Fig. 5. The MTM plates were fabricated by wire electrical discharge machining and postprocessed by electropolishing.

The MTM structure can support traveling waves with both negative effective permittivity and permeability [60].

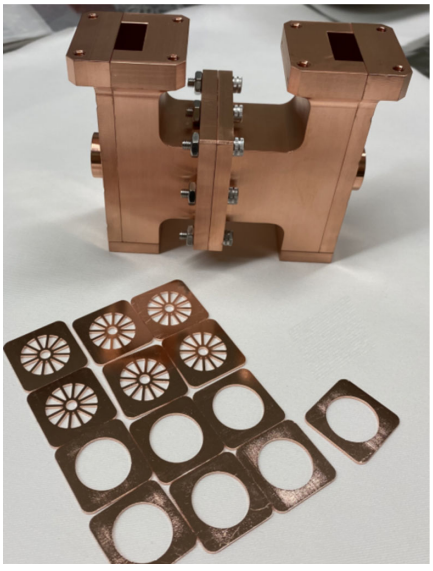

FIG. 5. Photo of the assembled metamaterial (MTM) structure with spare wagon wheel plates and spacer plates.

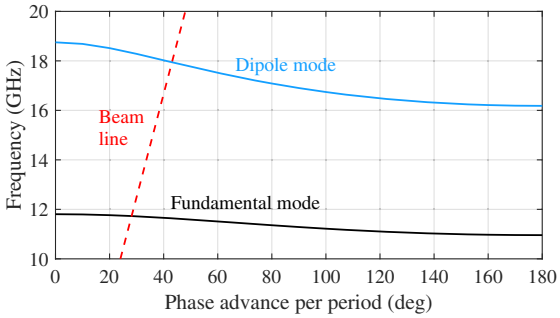

FIG. 6. Dispersion curves of the fundamental mode (black) and the dipole mode (blue) in the MTM structure. The fundamental mode intercepts with the relativistic electron beam line (red) $\omega = k_z v_z$ at 11.7 GHz, where ω is the angular frequency, k_z is the longitudinal wave number in the beam direction z, and v_z is the beam longitudinal velocity.

Figure 6 shows the dispersion curves of the fundamental mode and the dipole mode, both exhibiting negative group velocity.

Figure 7 shows the frequency spectra of the input and transmitted rf pulses centered at 11.7 GHz. The MTM structure is optimized for a high transient gradient, and the resulting bandwidth of the transmitted rf spectrum is slightly narrower than that of the input rf spectrum. This gives rise to the feature of a primary pulse and secondary pulses in the transmitted rf signal, which has enabled direct detection of the BIAR breakdown.

2. Low-power microwave measurements

Low-power microwave measurements were conducted before and after the high-power test. The rf transmission between the input and output ports was measured, represented by the magnitude of the S_{21} parameter. Figure 8 illustrates that the rf transmission exhibited a slight improvement after the high-power test, indicating the robustness of the MTM structure and the effect of rf conditioning.

3. Statistical analysis of breakdown events

A statistical analysis was performed, where we separated all the pulses into three types of events: nonbreakdown events, BIAR breakdown events, and destructive breakdown

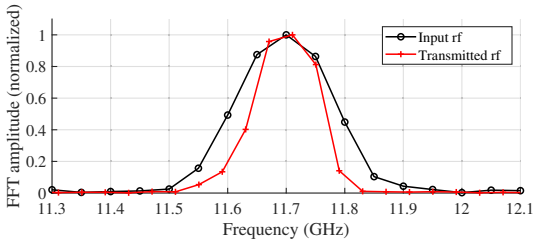

FIG. 7. Frequency spectra of the input (black) and transmitted (red) rf pulses.

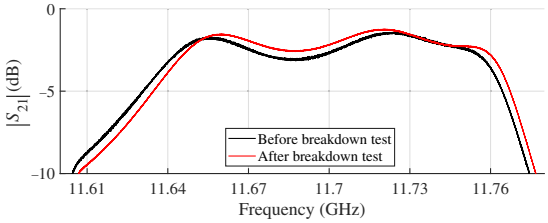

FIG. 8. Comparison of the rf transmission, as the magnitude of the S_{21} parameter, before and after the high-power breakdown test.

events. The classification of breakdown events was conducted by comparing the measured transmitted voltage with the theoretical reconstruction, as detailed as follows: (i) If a transmitted rf voltage waveform has two peaks (the primary pulse and the following secondary pulse), this event is identified as a nonbreakdown event. (ii) If a transmitted rf voltage waveform has only one primary pulse, while the measured peak voltage of the primary pulse is lower than the theoretically reconstructed peak voltage by over 5%, this event is identified as a destructive breakdown event. (iii) Otherwise (or if a transmitted rf voltage waveform has only one primary pulse, while the measured peak voltage of the primary pulse is greater than 95% of the theoretically

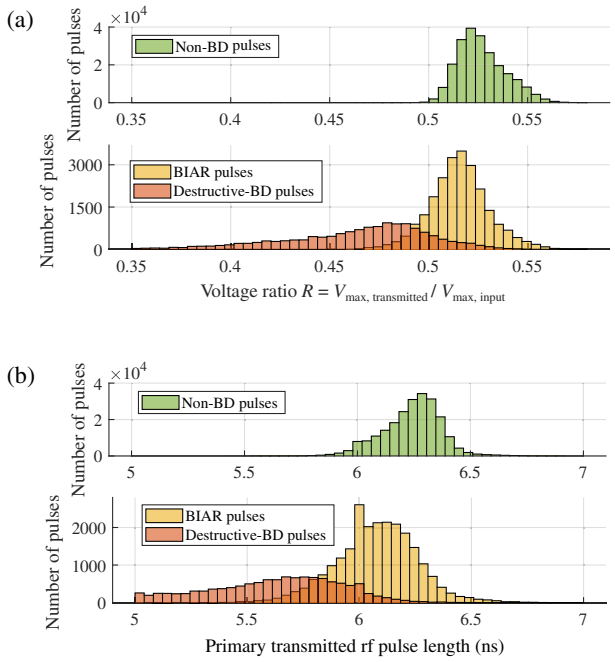

FIG. 9. Statistical analysis of the three types of breakdown events, namely nonbreakdown ("non-BD"), BIAR, and destructive breakdown ("destructive-BD") events. (a) Histograms of the ratio R between the transmitted peak rf voltage in the primary pulse $V_{\text{max,transmitted}}$ and the input rf voltage $V_{\text{max,input}}$. (b) Histograms of the full width at half maximum duration of the primary transmitted rf pulses.

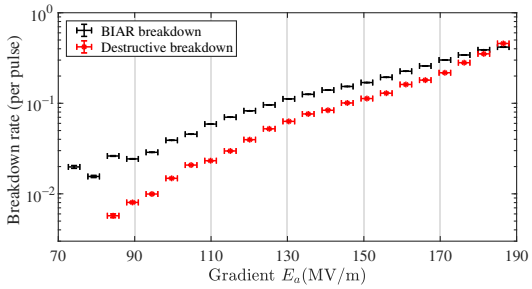

FIG. 10. Breakdown rates in the conditioning phase plotted against the gradient E_a.

reconstructed peak voltage), this event is identified as a BIAR breakdown event.

We show histograms of two key characteristics in the transmitted rf pulses in Fig. 9. Figure 9(a) shows the ratio R of the peak voltage between the transmitted rf voltage $V_{\text{max,transmitted}}$ (in the primary pulse) and the input rf voltage $V_{\text{max,input}}$ as $R = V_{\text{max,transmitted}}/V_{\text{max,input}}$, where the distribution of R for the BIAR events is similar to that for the nonbreakdown events. Figure 9(b) shows the duration of the primary transmitted rf pulse. Bimodal distributions are observed between the two breakdown types.

4. Breakdown rate in the conditioning phase

The breakdown rate (BDR) in the conditioning phase dataset is shown in Fig. 10. The BDR in the testing phase is lower than that observed in the conditioning phase, showing the effect of conditioning.

[1] E. R. Colby and L. K. Len, Rev. Accel. Sci. Techol. **09**, 1 (2016).

[2] S. Belomestnykh, G. Blazey, J. Byrd, B. Carlsten, A. Grassellino, A. Gurevich, E. Jensen, A. Lankford, W. Leemans, L. K. Len *et al.*, *Radiofrequency Accelerator R&D Strategy Report: DOE HEP General Accelerator R&D RF Research Roadmap Workshop, 2017* (2017), 10.2172/1631119.

[3] C. Adolphsen, D. Angal-Kalinin, T. Arndt, M. Arnold, R. Assmann, B. Auchmann, K. Aulenbacher, A. Ballarino, B. Baudouy, P. Baudrenghien *et al.*, European Strategy for Particle Physics—Accelerator R&D Roadmap, CERN Yellow Reports: Monographs, Report No. CERN-2022-001, Vol. **1**, 2022.

[4] C. Geddes, M. Hogan, P. Musumeci, and R. Assmann, Report of Snowmass 21 accelerator frontier topical group 6 on advanced accelerators, arXiv:2208.13279.

[5] F. Albert, M. E. Couprie, A. Debus, M. C. Downer, J. Faure, A. Flacco, L. A. Gizzi, T. Grismayer, A. Huebl, C. Joshi *et al.*, New J. Phys. **23**, 031101 (2021).

[6] C. Joshi, S. Corde, and W. B. Mori, Phys. Plasmas **27**, 070602 (2020).

[7] E. Esarey, C. B. Schroeder, and W. P. Leemans, Rev. Mod. Phys. **81**, 1229 (2009).

[8] A. J. Gonsalves, K. Nakamura, J. Daniels, C. Benedetti, C. Pieronek, T. C. H. de Raadt, S. Steinke, J. H. Bin, S. S. Bulanov, J. van Tilborg *et al.*, Phys. Rev. Lett. **122**, 084801 (2019).

[9] L. Rovige, J. Huijts, I. Andriyash, A. Vernier, V. Tomkus, V. Girdauskas, G. Raciukaitis, J. Dudutis, V. Stankevic, P. Gecys *et al.*, Phys. Rev. Accel. Beams **23**, 093401 (2020).

[10] A. Caldwell, E. Gschwendtner, K. Lotov, P. Muggli, and M. Wing (AWAKE Collaboration), AWAKE design report: A proton-driven plasma wakefield acceleration experiment at CERN, CERN Technical Report No. CERN-SPSC-2013-013, No. SPSC-TDR-003, 2013, https://inspirehep.net/literature/1614082.

[11] R. Assmann, M. Weikum, T. Akhter, D. Alesini, A. Alexandrova, M. Anania, N. Andreev, I. Andriyash, M. Artioli, A. Aschikhin *et al.*, Eur. Phys. J. Spec. Top. **229**, 3675 (2020).

[12] C. Jing, J. Power, J. Shao, G. Ha, P. Piot, X. Lu, A. Zholents, A. Kanareykin, S. Kuzikov, J. B. Rosenzweig *et al.*, Continuous and coordinated efforts of structure wakefield acceleration (SWFA) development for an energy frontier machine, arXiv:2203.08275.

[13] X. Lu, J. Shao, J. Power, C. Jing, G. Ha, P. Piot, A. Zholents, R. Temkin, M. Shapiro, J. Picard *et al.*, arXiv:2203.08374.

[14] CLIC, CLICdp Collaborations, The Compact Linear Collider (CLIC) 2018 Summary Report, arXiv:1812.06018.

[15] D. Yu, H. Henke, H. Braun, S. Dobert, and W. Wuensch, in *Proceedings of the 19th Particle Accelerator Conference, Chicago, IL, 2001* (IEEE, Piscataway, NJ, 2001), pp. 3858–3860.

[16] W. Wuensch, C. Achard, S. Dobert, H. Braun, I. Syratchev, M. Taborelli, and I. Wilson, in *Proceedings of the 20th Particle Accelerator Conference, PAC-2003, Portland, OR* (IEEE, New York, 2003), pp. 495–497.

[17] S. Döbert, in *Proceedings of the 22nd International Linear Accelerator Conference, LINAC-2004, Lübeck, Germany* (JACoW, Geneva, Switzerland, 2004), pp. 513–517.

[18] A. Grudiev, S. Calatroni, and W. Wuensch, Phys. Rev. ST Accel. Beams **12**, 102001 (2009).

[19] S. Matsumoto, T. Abe, Y. Higashi, T. Higo, and Y. Du, Nucl. Instrum. Methods Phys. Res., Sect. A **657**, 160 (2011).

[20] A. Degiovanni, W. Wuensch, and J. Giner Navarro, Phys. Rev. Accel. Beams **19**, 032001 (2016).

[21] I. Syratchev, G. Riddone, and S. Tantawi, in *Proceedings of the 11th European Particle Accelerator Conference, Genoa, Italy, 2008* (EPSAG, Geneva, 2008), pp. 1909–1911.

[22] A. Cappelletti, V. Dolgashev, J. Lewandoski, S. Tantawi, S. Weathersby, and J. Zelinski, Nucl. Instrum. Methods Phys. Res., Sect. A **657**, 78 (2011).

[23] J. Shao, C. Jing, E. Wisniewski, G. Ha, M. Conde, W. Liu, J. Power, and L. Zheng, Phys. Rev. Accel. Beams **23**, 011301 (2020).

[24] J. Picard, I. Mastovsky, M. A. Shapiro, R. J. Temkin, X. Lu, M. Conde, D. S. Doran, G. Ha, J. G. Power, J. Shao *et al.*, Phys. Rev. Accel. Beams **25**, 051301 (2022).

[25] M. Peng, M. Conde, G. Ha, C. Jing, W. Liu, J. Power, J. Seok, J. Shao, E. Wisniewski, and J. Shi, in *Proceedings of the 10th International Particle Accelerator Conference, IPAC'19, Melbourne, Australia* (JACoW, Geneva, Switzerland, 2019), pp. 734–737.

[26] S. Antipov, P. Avrakhov, V. Dolgashev, D. Doran, C. Jing, S. Kuzikov, W. Liu, J. Power, J. Shao, and E. Wisniewski, in *Proceedings of the 12th International Particle Accelerator Conference, IPAC-2021, Campinas, Brazil* (JACoW, Geneva, Switzerland, 2021), pp. 532–534.

[27] M. Dal Forno, V. Dolgashev, G. Bowden, C. Clarke, M. Hogan, D. McCormick, A. Novokhatski, B. Spataro, S. Weathersby, and S. G. Tantawi, Phys. Rev. Accel. Beams **19**, 051302 (2016).

[28] M. Dal Forno, V. Dolgashev, G. Bowden, C. Clarke, M. Hogan, D. McCormick, A. Novokhatski, B. Spataro, S. Weathersby, and S. G. Tantawi, Phys. Rev. Accel. Beams **19**, 011301 (2016).

[29] B. O'Shea, G. Andonian, S. Barber, K. Fitzmorris, S. Hakimi, J. Harrison, P. Hoang, M. Hogan, B. Naranjo, O. Williams *et al.*, Nat. Commun. **7**, 12763 (2016).

[30] J. Shao, H. Chen, D. Doran, G. Ha, C. Jing, X. Lin, W. Liu, M. Peng, J. Power, J. Shi *et al.*, in *Proceedings of the 13th International Particle Accelerator Conference, IPAC'22, Bangkok, Thailand* (JACoW, Geneva, Switzerland, 2022), pp. 3134–3137.

[31] W. H. Tan, S. Antipov, D. S. Doran, G. Ha, C. Jing, E. Knight, S. Kuzikov, W. Liu, X. Lu, P. Piot *et al.*, Phys. Rev. Accel. Beams **25**, 083402 (2022).

[32] J. Norem, Z. Insepov, and I. Konkashbaev, Nucl. Instrum. Methods Phys. Res., Sect. A **537**, 510 (2005).

[33] P. B. Wilson, in *Proceedings of the 12th Advanced Accelerator Concepts Workshop (AAC'06), Lake Geneva, WI* (American Institute of Physics, College Park, MD, 2006), pp. 27–40.

[34] K. L. Jensen, Y. Y. Lau, D. W. Feldman, and P. G. O'Shea, Phys. Rev. ST Accel. Beams **11**, 081001 (2008).

[35] G. S. Nusinovich, D. Kashyn, and T. M. Antonsen, Phys. Rev. ST Accel. Beams **12**, 101001 (2009).

[36] F. Djurabekova, S. Parviainen, A. Pohjonen, and K. Nordlund, Phys. Rev. E **83**, 026704 (2011).

[37] K. Nordlund and F. Djurabekova, Phys. Rev. ST Accel. Beams **15**, 071002 (2012).

[38] V. Zadin, A. Pohjonen, A. Aabloo, K. Nordlund, and F. Djurabekova, Phys. Rev. ST Accel. Beams **17**, 103501 (2014).

[39] E. Z. Engelberg, Y. Ashkenazy, and M. Assaf, Phys. Rev. Lett. **120**, 124801 (2018).

[40] W. Wuensch, in *Proceedings of the 8th European Particle Accelerator Conference, Paris, 2002* (EPS-IGA and CERN, Geneva, 2002), pp. 134–138.

[41] E. I. Simakov, V. A. Dolgashev, and S. G. Tantawi, Nucl. Instrum. Methods Phys. Res., Sect. A **907**, 221 (2018).

[42] J. Wang, RF properties of periodic accelerating structures for linear colliders, Ph.D. thesis, Stanford University, 1989.

[43] H. H. Braun, S. Döbert, I. Wilson, and W. Wuensch, Phys. Rev. Lett. **90**, 224801 (2003).

[44] V. Dolgashev, S. Tantawi, Y. Higashi, and B. Spataro, Appl. Phys. Lett. **97**, 171501 (2010).

[45] D. P. Pritzkau and R. H. Siemann, Phys. Rev. ST Accel. Beams **5**, 112002 (2002).

[46] L. Laurent, S. Tantawi, V. Dolgashev, C. Nantista, Y. Higashi, M. Aicheler, S. Heikkinen, and W. Wuensch, Phys. Rev. ST Accel. Beams **14**, 041001 (2011).

[47] R. A. Marsh, M. A. Shapiro, R. J. Temkin, V. A. Dolgashev, L. L. Laurent, J. R. Lewandowski, A. D. Yeremian, and S. G. Tantawi, Phys. Rev. ST Accel. Beams **14**, 021301 (2011).

[48] F. Wang, C. Adolphsen, and C. Nantista, Phys. Rev. ST Accel. Beams **14**, 010401 (2011).

[49] A. D. Cahill, J. B. Rosenzweig, V. A. Dolgashev, S. G. Tantawi, and S. Weathersby, Phys. Rev. Accel. Beams **21**, 102002 (2018).

[50] E. Senes, T. Argyropoulos, F. Tecker, and W. Wuensch, Phys. Rev. Accel. Beams **21**, 102001 (2018).

[51] B. J. Munroe, A. M. Cook, M. A. Shapiro, R. J. Temkin, V. A. Dolgashev, L. L. Laurent, J. R. Lewandowski, A. D. Yeremian, S. G. Tantawi, and R. A. Marsh, Phys. Rev. ST Accel. Beams **16**, 012005 (2013).

[52] T. Higo, Y. Higashi, S. Matsumoto, K. Yokoyama, C. Adolphsen, V. Dolgashev, A. Jensen, L. Laurent, S. Tantawi, F. Wang *et al.*, in *Proceedings of the International Particle Accelerator Conference, Kyoto, Japan, 2010* (ICR, Kyoto, 2010), pp. 3702–3704.

[53] X. Wu, J. Shi, H. Chen, J. Shao, T. Abe, T. Higo, S. Matsumoto, and W. Wuensch, Phys. Rev. Accel. Beams **20**, 052001 (2017).

[54] H. Xu, M. A. Shapiro, and R. J. Temkin, Phys. Rev. Accel. Beams **22**, 021002 (2019).

[55] S. Döbert, I. H. Wilson, W. Wuensch, M. Taborelli, C. Archard, I. Syratchev, S. T. Heikkinen, C. Adolphsen, and A. Grudiev, High gradient test of a clamped, molybdenum iris, X-Band accelerator structure at NLCTA, CERN, Geneva, Technical Report No. CERN-AB-2005-005, 2004.

[56] M. A. K. Othman, J. Picard, S. Schaub, V. A. Dolgashev, S. M. Lewis, J. Neilson, A. Haase, S. Jawla, B. Spataro, R. J. Temkin *et al.*, Appl. Phys. Lett. **117**, 073502 (2020).

[57] M. Schneider, V. Dolgashev, J. W. Lewellen, S. G. Tantawi, E. A. Nanni, M. Zuboraj, R. Fleming, D. Gorelov, M. Middendorf, and E. I. Simakov, Appl. Phys. Lett. **121**, 254101 (2022).

[58] S. Weatherly, D. Doran, B. Freemire, C. Jing, J. Power, and E. Wisniewski, in *Proceedings of 5th North American Particle Accelerator Conference, NAPAC'22, Albuquerque, NM* (JACoW, Geneva, Switzerland, 2022), pp. 52–54.

[59] Z. Duan, M. A. Shapiro, E. Schamiloglu, N. Behdad, Y. Gong, J. H. Booske, B. N. Basu, and R. J. Temkin, IEEE Trans. Electron Devices **66**, 207 (2019).

[60] R. Marqués, F. Martin, and M. Sorolla, *Metamaterials with Negative Parameters: Theory, Design, and Microwave Applications* (John Wiley & Sons, 2011).

[61] S. Antipov, L. Spentzouris, W. Liu, W. Gai, and J. G. Power, J Appl. Phys. **102**, 034906 (2007).

[62] T. P. Wangler, *RF Linear Accelerators* (John Wiley & Sons, New York, 2008).

[63] CST Studio Suite, https://www.3ds.com/products-services/simulia/products/cst-studio-suite/.

[64] J. T. Picard, High power microwave generation for advanced particle acceleration, Massachusetts Institute of Technology, Ph.D. thesis, 2022.

[65] B. C. Stuart, M. D. Feit, S. Herman, A. M. Rubenchik, B. W. Shore, and M. D. Perry, Phys. Rev. B **53**, 1749 (1996).

[66] R. H. Fowler and L. Nordheim, Proc. R. Soc. A **119**, 173 (1928).

[67] J. Wang and G. Loew, Stanford University, Stanford Linear Accelerator Center, CA, Field emission and rf breakdown in high-gradient room temperature linac structures, Technical Report No. SLAC-PUB-7684, 1997, https://inspirehep.net/literature/454313.

[68] R. Vaughan, IEEE Trans. Electron Devices **40**, 830 (1993).

[69] M. A. Furman and M. T. F. Pivi, Phys. Rev. ST Accel. Beams **5**, 124404 (2002).

[70] R. Cimino, I. R. Collins, M. A. Furman, M. Pivi, F. Ruggiero, G. Rumolo, and F. Zimmermann, Phys. Rev. Lett. **93**, 014801 (2004).

[71] M. Johnson, R. Ruber, V. Ziemann, and H. Braun, Nucl. Instrum. Methods Phys. Res., Sect. A **595**, 568 (2008).

[72] F. Wang and C. Adolphsen, Phys. Rev. ST Accel. Beams **12**, 042001 (2009).

[73] O. Etisken, F. Antoniou, Y. Papaphilippou, T. Tydecks, F. Zimmermann, A. K. Ciftci, and K. Oide, Phys. Rev. Accel. Beams **26**, 081601 (2023).

[74] G. D'Auria, N. Thompson, J. Clarke, M. Ferrario, W. Wuensch, F. Nguyen, A. Aksoy, R. Rochow, A. Chianchi, A. Latina *et al.*, Conceptual Design Report of the CompactLight X-ray FEL, CompactLight Partnership Technical Report No. XLS-Report-2021-010, 2021, https://inspirehep.net/literature/2659056.

[75] P. Piot, G. Chen, X. Lu, J. Power, E. Wisniewski, C. Jing, S. Kuzikov, and E. Frame, in *Proceedings of the (pre-press) 67th ICFA Advanced Beam Dynamics Workshop on Future Light Sources, FLS'23, Luzern, Switzerland* (JACoW, Geneva, Switzerland, 2023), MO4C2.

[76] J. Genoud, E. L. Claveau, S. K. Jawla, G. Li, J. F. Picard, M. A. Shapiro, and R. J. Temkin, Appl. Phys. Lett. **121**, 044101 (2022).

[77] O. A. Ivanov, M. A. Lobaev, A. L. Vikharev, A. M. Gorbachev, V. A. Isaev, J. L. Hirshfield, S. H. Gold, and A. K. Kinkead, Phys. Rev. Lett. **110**, 115002 (2013).

[78] G. Burt, S. V. Samsonov, K. Ronald, G. G. Denisov, A. R. Young, V. L. Bratman, A. D. R. Phelps, A. W. Cross, I. V. Konoplev, W. He, J. Thomson, and C. G. Whyte, Phys. Rev. E **70**, 046402 (2004).

[79] S. V. Samsonov, A. D. R. Phelps, V. L. Bratman, G. Burt, G. G. Denisov, A. W. Cross, K. Ronald, W. He, and H. Yin, Phys. Rev. Lett. **92**, 118301 (2004).